*Article*

# Monodispersed NiO Nanoparticles into SBA-15: An Efficient Nanocatalyst to Produce Ketone-Alcohol (KA) Oil by the Oxidation of Cyclohexane in Mild Conditions

Mohamed Abboud [1,*], Reem S. Alnefaie [1], Asla A. AL-Zahrani [2], Nabil Al-Zaqri [3], Mohammad Abu Haija [4], Azza Al-Ghamdi [2], Mabkhoot Alsaiari [5,6], Mohammed Jalalah [5,7], Omeer Albormani [1] and Mohamed S. Hamdy [1]

[1] Catalysis Research Group (CRG), Department of Chemistry, College of Science, King Khalid University, Abha 61413, Saudi Arabia
[2] Department of Chemistry, College of Science, Imam Abdulrahman bin Faisal University, Dammam 31441, Saudi Arabia
[3] Department of Chemistry, College of Science, King Saud University, Riyadh 11451, Saudi Arabia
[4] Department of Chemistry, Khalifa University of Science and Technology, Abu Dhabi 127788, United Arab Emirates
[5] Promising Centre for Sensors and Elezctronic Devices (PCSED), Advanced Materials and Nano Research Centre, Najran University, Najran 11001, Saudi Arabia
[6] Empty Quarter Reszearch Unit, Department of Chemistry, College of Science and Art in Sharurah, Najran University, Sharurah 68344, Saudi Arabia
[7] Department of Electrical Engineering, College of Engineering, Najran University, Najran 11001, Saudi Arabia
* Correspondence: abboud_med@yahoo.fr or mabboud@kku.edu.sa; Tel.: +966-53-48-46-782

**Abstract:** A simple and efficient approach to preparing highly efficient and reusable NiO@SBA-15 nanocatalysts for the oxidation of cyclohexane to produce ketone-alcohol (KA) oil was reported. These nanocatalysts were prepared by the dispersion of NiO NPs into SBA-15 using a coordination-assisted grafting method. In this approach, four commercially available nickel salts were immobilized into amino-functionalized SBA-15. After washing and calcination, four new nanocatalysts were obtained. The high dispersion of NiO NPs into SBA-15 was confirmed by HR-TEM and XRD. Different oxidants such as $O_2$, $H_2O_2$, *t*-butyl hydrogen peroxide (TBHP), and *meta*-Chloroperoxybenzoic acid (*m*-CPBA) were evaluated. However, *m*-CPBA exhibited the highest catalytic activity. Compared to different catalysts reported in the literature, for the first time, 75–99% of cyclohexane was converted to KA oil over NiO@SBA-15. In addition, the cyclohexane conversion and K/A ratio were affected by the reaction time, catalyst dose, Ni content, and NiO dispersion. Moreover, NiO@SBA-15 maintained a high catalytic activity during five successive cycles.

**Keywords:** cyclohexane oxidation; KA oil; monodispersed NiO NPs; amino-functionalized SBA-15; coordination-assisted grafting method; *m*-CPBA

## 1. Introduction

The oxidation reaction of cyclohexane (CXN) is one of the most important industrial processes. This reaction produces cyclohexanone (CXK) and cyclohexanol (CXA), which are together known as ketone-alcohol (KA) oil. KA oil is known as the main feedstock for the production of nylon 6 and 6,6 (Scheme 1). Because the additional oxidation of KA oil can afford the adipic acid, which is a key monomer for the synthesis of nylon 6,6 [1]. Moreover, adipic acid is a key intermediate in industrial organic chemistry [2,3].

The current industrial process to prepare KA oil requires the utilization of manganese or cobalt salts as homogenous catalytic systems for the oxidation of CXN. Because of the high stability of CXN, and the high activation energy of its C-H bonds, the industrial operating conditions for its oxidation are drastic. The industrial production of KA oil

by oxidation of CXN under air or molecular oxygen requires high pressure (10–20 atm) and elevated temperature (150–160 °C). However, because the suitable products, CXK and CXA, are not much more stable than the CXN, numerous by-products can be formed under elevated pressure and temperature. Consequently, at the high conversion of CXN, the selectivity of KA oil decreases, which makes KA oil purification difficult and a costly process. Therefore, to increase the KA oil selectivity to 70–85%, the conversion of CXN must be maintained in the range of 4–6% [4]. Moreover, the utilization of a homogeneous catalytic system, which cannot be regenerated and reused, makes the oxidation process of CXN to prepare KA oil an inefficient and expensive industrial process.

To improve the oxidation process of CXN, many homogeneous and heterogeneous catalytic systems have been developed in the last 20 years [5–21]. However, these catalysts converted the CXN with low conversion (<30%) to maintain reasonable KA selectivity. Various organometallic complexes were also evaluated as homogeneous catalysts for the oxidation of CXN using different types of oxidants, such as $t$-butyl hydrogen peroxide (TBHP) [5,6] and $H_2O_2$ [7–9]. However, the best results were reported by Alshaheri et al., with around 30% conversion and very high selectivity (around 98%) [9].

Due to the drawbacks of a homogeneous catalysis, such as non-possible regeneration and reutilization of the catalyst, and difficult separation and purification of the products, heterogeneous catalysis can be considered an ideal alternative. Therefore, numerous heterogeneous catalysts have been reported during the last two decades [4,10–20,22–30]. Most of these catalytic systems are metal-based catalysts, such as Au [4,16,17,22,25,27], Ti [4,16,23], Ag [10,19,24], Co [12,14,23,25,27,29], Mo [20], Fe [14,25,27,29], Mn [13,14,25], Cr [14,27,28], and V [15], and even lanthanides-based catalysts such as Ce [11,27,30], La [30], Sm [30], Dy [30], Y [30], and Gd [30]. These metals were supported in different solid matrices such as silica [4,10,24–28], zeolites [4,12–14,22,27,29], aluminophosphates (AlPo) [15,25,27,29,30], alumina [22], graphite [17], carbon nanotubes [18], metal oxides [19], and MOFs [20]. According to these reported catalytic systems, the high dispersion of the appropriate metal NPs in a high surface area solid matrix can improve the conversion and selectivity of the oxidation reaction of CXN. For example, Xu et al. [4] reported the utilization of titania-doped silica-supported gold NPs (50 mg) as a catalyst under air, high pressure (1.5 MPa), and temperature (150 °C). However, only 9.2% of CXN (20 mL) was transformed into KA oil. Under similar conditions Li-Xin et al. [22] reported the conversion of 10–13% of CXN (20 mL) with high KA oil selectivity (84–87%) over alumina-supported gold (50 mg of 0.2–1.0% Au/$Al_2O_3$), using $O_2$ as oxidant. Using SBA-15 mesoporous silica as a support of gold NPs, and under similar conditions, Wu et al. [25] obtained 16.6% CXN conversion with 92.4% selectivity. Wang et al. [26] obtained similar results (16.9% CXN conversion, 93% KA oil selectivity) using SBA-15 supported bismuth (40 mg containing 0.5, 0.8, 1.2 or 1.9 wt% of Bi in Bi-SBA-15) with 8 mL of CXN, using $O_2$ as oxidant. However, supported gold in mild conditions showed lower conversion and selectivity. As reported by Enache et al. [17], only 2–7% of CXN conversion with 10–23% KA oil selectivity was obtained when graphite-supported gold (0.5, 1 and % of Au/graphene) was applied as a catalyst at 70 °C and 1 atm, using 10 mL of CXN and 0.12 g of the catalyst, with 0.08 g of TBHP as oxidant.

All these developed catalytic systems mentioned above still have many drawbacks, such as low CXN conversion at high KA oil selectivity, expensive or toxic metals (i.e., Au, Cr), and high-cost processes (i.e., high temperature, high pressure). Hence, the production of KA oil from the oxidation of CXN in mild conditions, with high CXN conversion and KA oil selectivity, is still a concrete challenge.

Nickel is one of the most promising transition metals, as it is abundant, not toxic, and inexpensive metal. Moreover, Ni NPs possess unique electronic, mechanical, and optical properties that allow them to be investigated in various potential applications, including catalysis [31–34]. Recently, Ni NPs catalysts have been used as catalysts for many chemical transformations, such as aromatics hydrogenation [35], hydrocarbons oxidation [36–38], synthesis gas production [39], steam reforming [40], methanation [41], hydrocarbons isomerization [42], and hydrocracking [43–45]. However, the reported catalytic systems

still suffer from the low dispersion and high aggregation of Ni NPs, low conversion and selectivity, and low stability.

The focus of this work is the development of an efficient and recyclable catalytic system for selective oxidation of CXN to KA oil with high conversion in mild conditions. By combining the advantages of nickel NPs (mentioned above) and SBA-15 mesoporous silica as excellent catalyst support (i.e., high surface area, 2D hexagonal mesopores network, narrow pore size distribution, highly ordered nanostructure, easily functionalizable surface, and tunable pore diameter), we report here a new approach to prepare highly dispersed NiO NPs supported on SBA-15.

As shown in Scheme 1, (3-Aminopropyl)triethoxysilane (APTES) can be easily grafted into SBA-15, followed by the immobilization of nickel precursor [Ni] into silica surface via Ni—$NH_2$ coordination bonds. Then, mono-dispersed [Ni] molecules through silica surface ([Ni]@N-SBA-15) can be obtained after washing the as-made material with an appropriate solvent to remove all free molecules of [Ni]. Finally, the desired nanocatalyst NiO@SBA-15 can be generated by calcination. Using this approach, four nanocatalysts were prepared from four commercially available nickel precursors (i.e., nickel acetate, nickel nitrate, nickel chloride, and nickel sulfate), fully characterized and evaluated in the oxidation reaction of CXN to produce KA oil using different oxidants.
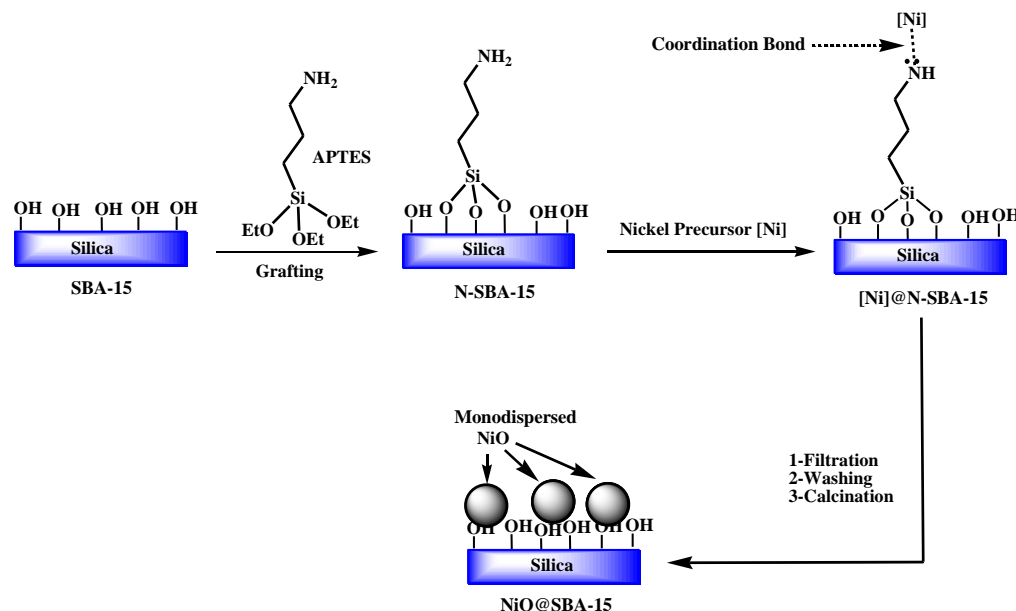


**Scheme 1.** Synthesis approach of mono-dispersed NiO NPs into SBA-15 (NiO@SBA-15).

## 2. Experimental Section

### 2.1. Materials

SBA-15 (pore size = 8 nm, particles size $\leq$ 150 μm), 3-aminopropyltriethoxysilane (APTES) (99%), absolute ethanol (99.8%), toluene (99.5%), nickel (II) nitrate ($Ni(NO_3)_2 \cdot 6H_2O$,) (98.5%), nickel (II) acetate ($Ni(CH_3CO_2)_2 \cdot 4H_2O$) (98%), nickel (II) chloride ($NiCl_2 \cdot 6H_2O$) (99.9%), nickel (II) sulfate ($NiSO_4 \cdot 6H_2O$) (98%), cyclohexane (99.5%), cyclohexanone (99.8%), cyclohexanol (99%), acetonitrile (99.9%), cylinder of molecular oxygen ($O_2$) (99.9%), hydrogen peroxide solution ($H_2O_2$) 30% (wt.) in $H_2O$, *t*-butyl hydrogen peroxide (TBHP) (5.0–6.0 M in decane), *meta*-chloroperoxybenzoic acid (*m*-CPBA) ($\leq$77%), dodecane ($\geq$99%), and magnesium sulfate $MgSO_4$ ($\geq$99.5%) were all supplied by Bayouni Trading Company (Jeddah, Saudi Arabia), which is the representant of Sigma Aldrich (St. Louis, MO, USA), and used without further purification.

## 2.2. Synthesis of the Catalysts

### 2.2.1. Synthesis of Amin-Functionalized Mesoporous Silica N-SBA-15

Following a procedure reported previously by Abboud et al. [46,47]. Briefly, 2 g of a commercial mesoporous silica SBA-15 were dispersed in 260 mL of toluene, then 0.7 mL of APTES was added slowly. The obtained mixture was stirred between 65–70 °C overnight. The obtained solid was filtered and washed thoroughly (three times) with absolute ethanol to remove the unreacted molecules of APTES. Finally, the obtained product was dried at 80–100 °C for 15 h.

### 2.2.2. Typical Procedure for the Synthesis of Nickel Precursors Coordinated to Amino-Functionalized SBA-15 [Ni]$_i$@N-SBA-15

Following a method described by Abboud et al. [46,47], briefly, 1 g of the nickel precursor [Ni]$_i$ {i = Ac for Ni(CH$_3$CO$_2$)$_2$·4H$_2$O; i = Nt for Ni(NO$_3$)$_2$·6H$_2$O; i = Cl for NiCl$_2$·6H$_2$O; i = Sl for NiSO$_4$·6H$_2$O} was dissolved in 200 mL of ethanol (ethanol/water: 100 mL/100 mL were used for NiSO$_4$·6H$_2$O), then 1 g of N-SBA-15 was added to the mixture. The obtained mixture was stirred for 15 h at 90 °C. The desired products [Ni]$_i$@N-SBA-15 (i = Ac, Nt, Cl or Sl) were obtained after filtration, washing with ethanol, then distilled water to remove all free molecules of the nickel precursor, and drying overnight at 100 °C.

### 2.2.3. Synthesis of SBA-15 Supported Nickel Oxide NiO$_i$@SBA-15

To obtain the desired catalysts NiO$_i$@SBA-15 (i = Ac, Nt, Cl or Sl), the four catalysts precursors [Ni]$_i$@N-SBA-15 were calcined under air for 5 h at 500 °C.

## 2.3. Catalytic Activity Evaluation

### 2.3.1. Oxidation of Cyclohexane over Bulk NiO: Conditions Optimization

To determine the optimal conditions for the oxidation of CXN, different parameters were investigated, such as reaction temperature, catalyst dose, reaction time, and the oxidant. For comparison purposes, unsupported bulk NiO (prepared by calcination of nickel nitrate at 500 °C under air 5 h) was used as a catalyst.

To determine the best oxidant among O$_2$, H$_2$O$_2$, TBHP, and *meta*-chloroperoxybenzoic acid (*m*-CPBA), extreme conditions of the temperature (≤70 °C to avoid the evaporation of CXN in solution), reaction time (24 h), and the catalyst amount (50 mg) used in the literature for liquid phase reaction [21] were the starting point. Since the best results were obtained with *m*-CPBA, other parameters were studied using *m*-CPBA as an oxidant. Here are the experimental conditions used for each oxidant. Oxidation reactions were monitored by gas chromatography (GC). The dodecane was used as an internal reference. Each oxidation reaction was run twice, and the average conversion and selectivity were determined and presented.

#### Using Hydrogen Peroxide (H$_2$O$_2$) as Oxidant

The oxidation of cyclohexane over bulk NiO using H$_2$O$_2$ was performed according to a method described previously by Abboud et al. [48]. 2 mL (18.5 mmol) of CXN and 4.2 mL (18.5 mmol) of dodecane (internal reference) and 10 mL of acetic acid were added to a mixture of 50 mg of NiO dispersed in 10 mL of acetic acid. After stirring the mixture for 5 min at 70 °C, 2.7 mL of H$_2$O$_2$ was added slowly. After stirring the mixture for 24 h at 70 °C, n-hexane was added to extract the organic layer. This later was dried over MgSO$_4$, and a sample of about 30 μL was taken, filtered in a hydrophobic membrane, and injected in GC.

#### Using Molecular Oxygen (O$_2$) as Oxidant

The oxidation of CXN over bulk NiO using molecular O$_2$ as an oxidant was performed in a high-pressure reactor vessel with a solvent-free process, following a modified procedure reported by Li et al. [30]. Briefly, 12 mL of CXN, 10 mL of dodecane (reference), and 20 mg

of bulk NiO were added into a high-pressure reactor vessel. After closing the reactor, the temperature was increased to 140–150 °C (0.5 MPa) with stirring. After stirring the obtained mixture for 24 h, the heating was turned off, and a sample of 30 μL was taken, at room temperature, filtered via a hydrophobic membrane, and injected in GC.

Using Tert-Butyl Hydroperoxide (TBHP) as Oxidant

Following a method described previously by Enache et al. [17], 0.12 mL of CXN and 0.1 mL of dodecane (reference) were added to a mixture of 50 mg of bulk NiO dispersed in 10 mL of acetonitrile. After stirring the mixture at 70 °C for 5 min, 0.3 mL of the oxidant TBHP was added. After stirring 24 h at 70 °C, a sample of around 30 μL was taken from the mixture, filtered via a hydrophobic membrane, and injected in GC.

Using-Chloroperoxybenzoic Acid (*m*-CPBA) as Oxidant

According to a procedure described previously by Enache et al. [17], shortly, 0.12 mL of CXN and 0.1 mL of dodecane (reference) were added to a mixture of 50 mg of bulk NiO dispersed in 10 mL of acetonitrile. After stirring the obtained mixture at 70 °C for 5 min, 1.5 eq of *m*-CPBA (288 mg) was added all at once. After stirring the mixture at 70 °C for 24 h, a sample of 30 μL was taken, filtered via a hydrophobic membrane, and injected in GC.

### 2.3.2. The Optimization of the Oxidation of CXN over Bulk NiO Using *m*-CPBA

The effect of the catalyst dose, reaction temperature, and reaction time was investigated using the procedure described in the part of Using *meta*-Chloroperoxybenzoic Acid (*m*-CPBA) as Oxidant above and the values listed in the following table (see Table 1).

**Table 1.** Investigated values of the catalyst dose, reaction temperature, and reaction time.

| Catalyst Dose (mg) | Temperature (°C) | Reaction Time (h) |
|---|---|---|
| 5, 10, 30, 50, 100 | 25, 40, 60, 70 °C | 0.5, 1, 2, 4, 24 |

### 2.3.3. General Procedure Used for the Oxidation of Cyclohexane over SBA-15 Supported NiO NPs (NiO$_i$@SBA-15)

The oxidation of CXN over NiO$_i$@SBA-15 using *m*-CPBA as oxidant was performed following the same procedure described above for bulk NiO. Briefly, 0.12 mL of CXN and 0.1 mL of dodecane (reference) were added to a mixture of 50 mg of NiO$_i$@SBA-15 dispersed in 10 mL of acetonitrile. After stirring the obtained mixture at 70 °C for 5 min, 1.5 eq of *m*-CPBA (288 mg) was added all at once. After stirring the mixture at 70 °C for 24 h, a sample of 30 μL was taken, filtered via a hydrophobic membrane, and injected in GC.

$$\text{Conversion (\%)} = 100 - \frac{\text{Peak area of cyclohexane}}{\text{Peak areas of (cyclohexane + all products)}} \times 100 \quad (1)$$

Equation (1): Conversion of cyclohexane (CXN) calculation

$$\text{Selectivity to CXK (\%)} = \frac{\text{Peak area of cyclohexanone}}{\text{Peak areas of all products}} \times 100 \quad (2)$$

Equation (2): Selectivity to cyclohexanone (CXK) calculation

$$\text{Selectivity to CXA (\%)} = \frac{\text{Peak area of cyclohexanol}}{\text{Peak areas of all products}} \times 100 \quad (3)$$

Equation (3): Selectivity to cyclohexanol (CXA) calculation

### 2.3.4. Catalyst Reusability

The bulk NiO was recycled as a catalyst in 5 successive runs following the procedure described above for *m*-CPBA (in the part of Using *meta*-Chloroperoxybenzoic Acid (*m*-CPBA) as Oxidant). While only the best catalyst among NiO$_i$@SBA-15 (i = Ac, Nt, Cl or Sl), which provided the highest conversion of CXN, was reused in 5 successive runs

following the method described above (Section 2.3.3). The best catalyst in this work was NiO$_{Ac}$@SBA-15. Briefly, the spent catalyst of the first run was recovered by filtration in a centrifuge, washed 3 times with CHCl$_3$ to remove the residual products, substrate, *m*-CPBA, internal reference, solvent, and *meta*-chlorobenzoic acid (*m*-CBA) produced after the decomposition of *m*-CPBA. After drying overnight at 100 °C, the recycled catalyst is ready to be used in the further cycle. This treatment was performed after each cycle.

### 2.4. Characterization Methods

The morphology of the synthesized nanomaterials was studied by a Scanning Electron Microscopy (SEM) Philips EM300, Siemens Autoscan, (Munchen, Germany), and a Transmission Electron Microscopy (TEM) FEI Tecnai G2 F30 TEM, operating at 200 kV. The powder X-ray diffraction (XRD) was performed on Shimadzu Lab-XRD–6000 with a secondary monochromator and CuK$\alpha$ radiation. The thermal behavior of the prepared material was studied by Thermogravimetric Analysis (TGA) and differential thermal analysis (DTA) under air, using a STARe system thermogravimetric analyzer, operating at a rate of 50 mL of air per minute, and samples were heated at 10 K min-1 from 25 to 800 °C. N$_2$ physisorption measurements were performed in Micrometrics ASAP 2010 apparatus (Norcross, GA, USA). The oxidation reaction of cyclohexane over the prepared nanocatalysts was monitored by gas chromatography (GC) type Shimadzu GC-17A, with RTX-5 column, 30 m × 0.25 mm, and 1 μm film thickness, and equipped with a flame ionization detector. Helium was used as a carrier gas at a flow rate of 0.6 mL/min, with a total flow of 100 mL/min, injector temperature of 160 °C, and detector temperature of 200 °C. Samples of about 30 μL were periodically withdrawn from the reaction mixture, and the volume injected was around 1 μL. FT-IR (infrared) spectra were recorded with KBr discs on Shimadzu FT-IR 3600 FT spectrophotometer. The nickel content in NiO@SBA-15 nanocatalysts was measured using the inductively coupled plasma spectrometry (ICP-AES), model 6500 (Thermo Scientific, Waltham, MA, USA).

## 3. Results and Discussion

### 3.1. Synthesis

To obtain highly dispersed and confined Ni NPs with quantized size, we developed a new method based on the immobilization of four commercially available nickel precursors, nickel acetate (Ac), nickel nitrate (Nt), nickel chloride (Cl), and nickel sulfate (Sl), in the surface of the SBA-15 through coordination-assisted grafting method. Following a procedure previously described by Abboud et al. [46,47], NiO$_i$@SBA-15 (i = Ac, Nt, Cl, or Sl) nanocatalysts were prepared in three main steps. In the first step, the amino-functionalized SBA-15 (N-SBA-15) was prepared via the grafting of APTES in the SBA-15 surface. In the second step, 1.1 eq of the nickel precursor for 1 eq of APTES was dissolved in ethanol and incorporated into SBA-15 to be coordinated with the amine groups of APTES. Due to the low solubility of nickel sulfate in ethanol, a mixture of EtOH/H$_2$O (1:1 *v/v*) was used to prepare [Ni]$_{Sl}$@N-SBA-15. These four different nickel precursors were used in this work to investigate the nickel precursor effect on NiO NPs' size, distribution, and catalytic activity. The excess of [Ni]$_i$ (free molecules) not coordinated to APTES was removed by extensive washing using ethanol and water. In the last step, the obtained catalysts precursors [Ni]$_i$@N-SBA-15 (i = Ac, Nt, Cl or Sl) were calcined at 500 °C for 5 h under air to obtain the final catalysts NiO$_i$@SBA-15 (i = Ac, Nt, Cl or Sl).

### 3.2. Characterization

Different techniques were used to characterize N-SBA-15, catalysts precursors [Ni]$_i$@N-SBA-15, and the final nanocatalysts NiO$_i$@SBA-15, such as FT-IR, BET, TEM, SEM, EDX, TGA/DTA, XRD, and ICP.

### 3.2.1. Fourier-Transform Infrared Spectroscopy (FT-IR)

The amino-functionalized SBA-15 (N-SBA-15) was synthesized following a method reported previously by Abboud et al. [46]. The grafting of APTES into the SBA-15 surface was confirmed by FT-IR spectroscopy (Figure S1, Table S1). The two peaks at 798 cm$^{-1}$ (●) and 1056 cm$^{-1}$ (■) in the SBA-15 curve are attributed to the symmetric and asymmetric stretching vibrations of Si–O, respectively. While the intensity of the SiO–H bending peak (□) at about 996 cm$^{-1}$ and SiO–H stretching broad peak (▲) at 3464 cm$^{-1}$ in the SBA-15 curve were obviously decreased in N-SBA-15, and the values are shifted to 970 cm$^{-1}$ and 3428 cm$^{-1}$, respectively. New bands appeared in the N-SBA-15 spectrum. The band at 2932 cm$^{-1}$ corresponds to CH$_2$ groups (○) of the APTES propyl chain, the band at 730 cm$^{-1}$ is assigned to the wagging vibration of N–H (♦), and the band at 1550 cm$^{-1}$ is assigned to scissoring vibration of N-H (◊). The band corresponding to the asymmetric and symmetric stretching vibration of N-H was not observed clearly. The bands observed at 1633 cm$^{-1}$ and 1637 cm$^{-1}$ in the SBA-15 and N-SBA-15 samples, respectively, are attributed to the –OH (Δ) deformation band [49]. Based on these observations and according to the previous study [46], we deduced that the grafting APTES into the SBA-15 surface was successful.

The obtained FT-IR spectra of the four catalysts precursors [Ni]$_i$@N-SBA-15 obtained after the incorporation of the nickel precursors [Ni]$_i$, are presented in Figure S2 and Table S2. The band of N-H assigned to in-plane bending (scissoring) (◊) shifted from 1550 cm$^{-1}$ to a lower frequency after the addition of nickel precursors to prepare [Ni]i@N-SBA-15. This can be due to the formation of a coordinate bond between the vacant orbitals of the nickel (II) ion and the lone pair electrons of NH$_2$. In addition, the intensity of the band attributed to C-H groups (○) at 2928 cm$^{-1}$ in [Ni]$_{Ac}$@N-SBA-15 spectrum increased compared to the intensity of the same band in the N-SBA-15 spectrum. This can be due to the additional band of CH$_3$ groups in the acetate. Based on these findings, we concluded that the nickel precursors [Ni]i (i = Ac, Nt, Cl, Sl) are successfully immobilized into N-SBA-15.

After the calcination of the four catalysts precursors [Ni]$_i$@N-SBA-15 at 500 °C for 5 h, all bands assigned to CH$_2$ and NH$_2$ disappeared (Figure 1 and Table 2). This is due to the decomposition of all organic groups and the formation of NiO$_i$@SBA-15 materials.
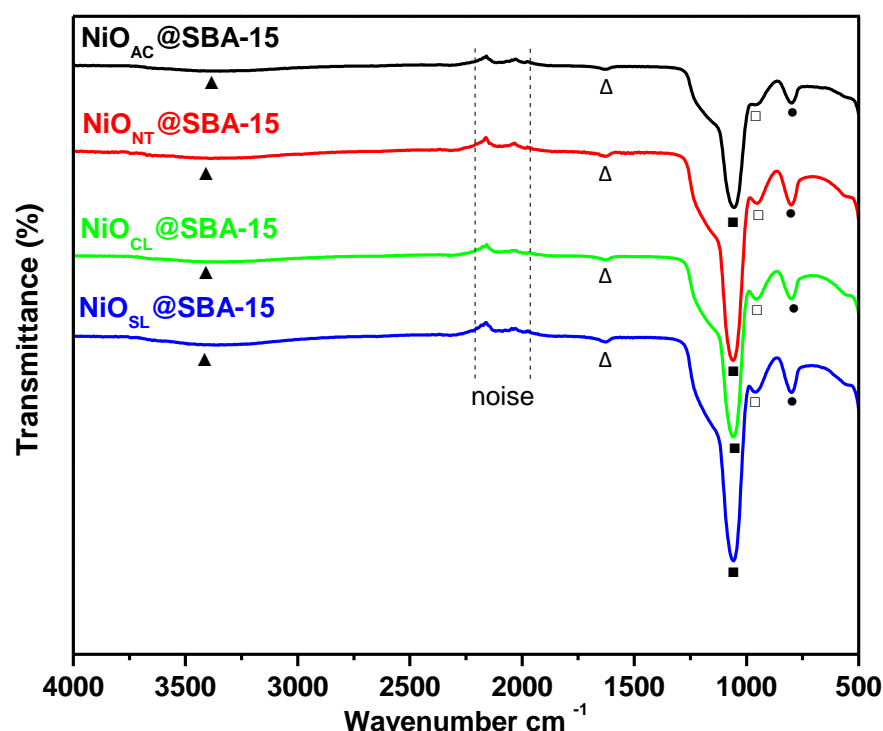


**Figure 1.** FT-IR spectra of four catalysts NiO$_j$@SBA$-$15 (j = AC, NT, CL, or SL). ▲: SiO-H stretching, Δ: SiO-H deformation, □: SiO-H bending, ●: Si-O Symmetric, ■: Si-O asymmetric, ○: CH2 of APTES, ♦: N-H out-plane bending, and ◊: N-H in-plane bending.

**Table 2.** FT-IR data of the prepared catalysts NiO$_i$@SBA-15.

| | Samples | υ SiO-H Str. (▲) (cm$^{-1}$) | υ SiO-H Deform. (Δ) (cm$^{-1}$) | υ SiO-H Bend. (□) (cm$^{-1}$) | υ Si-O Sym. (●) (cm$^{-1}$) | υ Si-O Asym. (■) (cm$^{-1}$) | υ CH$_2$ (APTES) (○) (cm$^{-1}$) | υ N-H Out-Plane Bend. (♦) (cm$^{-1}$) | υ N-H In-Plane Bend. (◊) (cm$^{-1}$) |
|---|---|---|---|---|---|---|---|---|---|
| Catalysts | NiO$_{Ac}$@SBA-15 | 3410 | 1627 | 977 | 801 | 1056 | - | - | - |
| | NiO$_{Nt}$@SBA-15 | 3410 | 1631 | 981 | 798 | 1060 | - | - | - |
| | NiO$_{Cl}$@SBA-15 | 3413 | 1627 | 988 | 798 | 1060 | - | - | - |
| | NiO$_{Sl}$@SBA-15 | 3417 | 1630 | 989 | 798 | 1060 | - | - | - |

str.: stretching; bend.: bending; sym.: symmetric; asym.: asymmetric.

### 3.2.2. Thermogravimetric Analysis and Differential Thermal Analysis of [Ni]i@N-SBA-15 (i = Ac, Nt, Cl and Sl) Precursors

Figure S3 illustrates the thermogravimetric analysis (TGA) and differential thermal analysis (DTA) results of precursors [Ni]$_i$@N-SBA-15 (i = Ac, Nt, Cl, and Sl). All samples show two discrete weight losses. The first weight loss observed below 180 °C for all samples' TGA curve (Figure S3a) is attributed to the physically adsorbed water, which is present at around 5%. This evaporation of the lattice and absorbed water is also observed in the differential thermal analysis (DTA) (Figure S3b) by endothermic peaks. The second weight loss was observed after 200 °C corresponded to the decomposition of acetate, nitrate, chloride, sulfate, and other organic residuals, such as APTES propylamine (PA) groups which decompose between 330 °C and 450 °C [46]. This weight loss exhibited corresponding endothermic peaks in DTA analysis. For the precursor [Ni]$_{Ac}$@N-SBA-15, the weight loss was observed at 230–400 °C with maximum weight loss at 350 °C, corresponding to about 4.0%. Similar thermal behavior was observed for the sulfate precursor [Ni]$_{Sl}$@N-SBA-15 at almost the same temperature range of 190–419 °C, with a maximum weight loss at 350 °C, and with about 4.1% weight loss. For the nitrate precursor [Ni]$_{Nt}$@N-SBA-15, this weight loss occurred at the larger temperature range of 170–460 °C with lower maximum weight loss at 295 °C and around 4.2% weight loss. The decomposition of chloride ions in precursor [Ni]$_{Cl}$@N-SBA-15 occurred at 250–470 °C with a maximum weight loss at 295 °C, corresponding to about 8.0%. The weight loss observed up to 800 °C can be related to the condensation reaction between the silanol groups of the silica surface [46].

In order to determine the nickel content with higher precision, all prepared catalysts NiO$_i$@SBA-15 (i = Ac, Nt, Cl, and Sl) were subjected to ICP analysis, and the obtained results are presented in Table 3.

**Table 3.** Nickel content in SBA-15 supported NiO determined by ICP.

| Catalysts | Nickel Content (wt. %) |
|---|---|
| NiO$_{Ac}$@SBA-15 | 7.26 |
| NiO$_{Nt}$@SBA-15 | 3.66 |
| NiO$_{Cl}$@SBA-15 | 4.03 |
| NiO$_{Sl}$@SBA-15 | 5.55 |

### 3.2.3. X-ray Powder Diffraction (XRD)

Powder XRD was performed for samples NiO$_i$@N-SBA-15 (i = Ac, Nt, Cl, and Sl) and for bulk NiO to investigate the dispersion degree of NiO particles through a silica framework. Figure 2 presents the obtained XRD patterns.
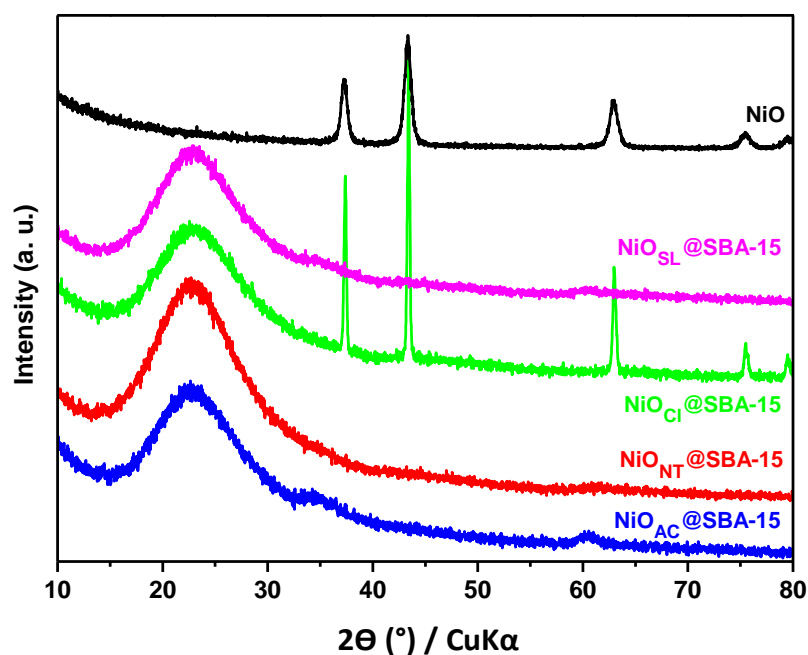
**Figure 2.** XRD patterns of materials NiO$_i$@SBA-15 (i = Ac, Nt, Cl, and Sl) and bulk NiO.

The XRD pattern of bulk NiO illustrates the main peaks of NiO at 2θ = 37.31°, 43.41°, 62.87°, 75.53°, and 79.46°, and are attributed to the planes (111), (200), (220), (311), and (222), respectively [50]. The XRD patterns of all SBA-15 mesoporous silica-supported NiO materials show a broad peak at about 2θ = 22.6°, which is a characteristic of amorphous silica materials. The absence of any crystalline phases for the three materials prepared from nickel acetate, nickel nitrate, and nickel sulfate, NiO$_i$@N-SBA-15 (i = Ac, Nt and Sl), indicates high dispersion of NiO particles through the silica surface. However, the XRD pattern of the material obtained from chloride precursor NiO$_{Cl}$@N-SBA-15 clearly shows the XRD pattern of NiO, indicating the low dispersion and higher aggregation of NiO particles. This is consistent with the results obtained previously by Kaydouh and coworkers [51].

### 3.2.4. N$_2$ Adsorption/Desorption

The N$_2$ physisorption isotherms and pore size distribution curves of the final catalysts NiO$_i$@SBA-15 (i = Ac, Nt, Cl, and Sl), the catalysts precursors [Ni]$_i$@N-SBA-15, N-SBA-15, and SBA-15 are presented in Figures 3 and 4, and Table 4.
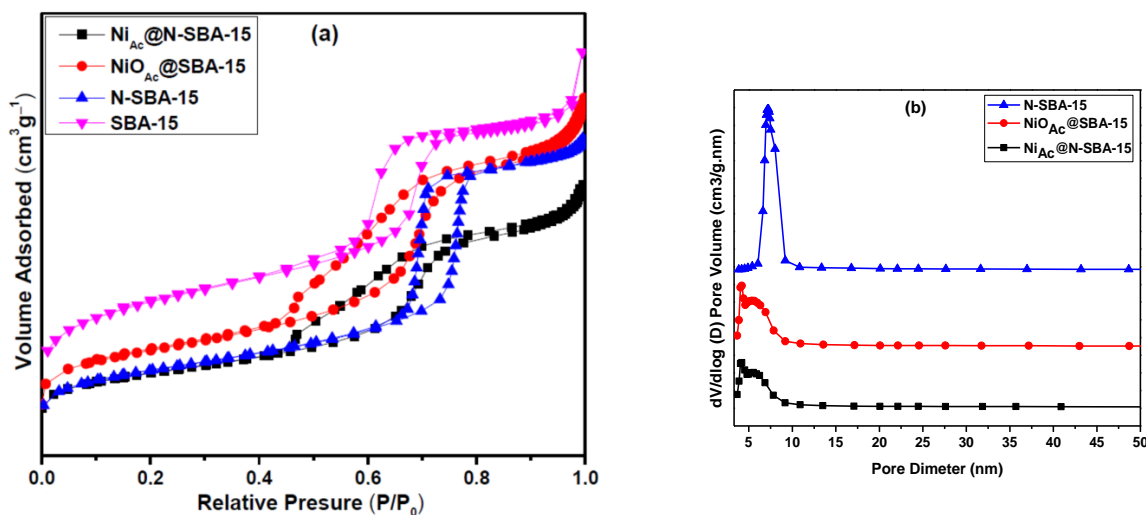


**Figure 3.** *Cont.*

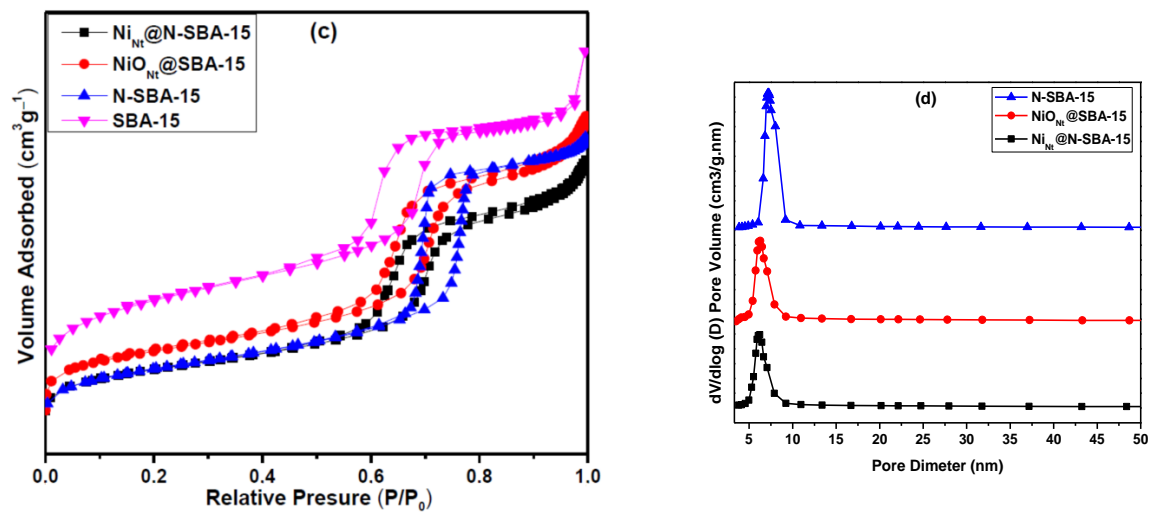**Figure 3.** N$_2$ physisorption isotherms (**a**,**b**) and pore size distributions (**c**,**d**) of SBA-15, N-SBA-15, [Ni]$_i$@N-SBA-15, NiO$_i$@SBA-15 (i = Ac and Nt).
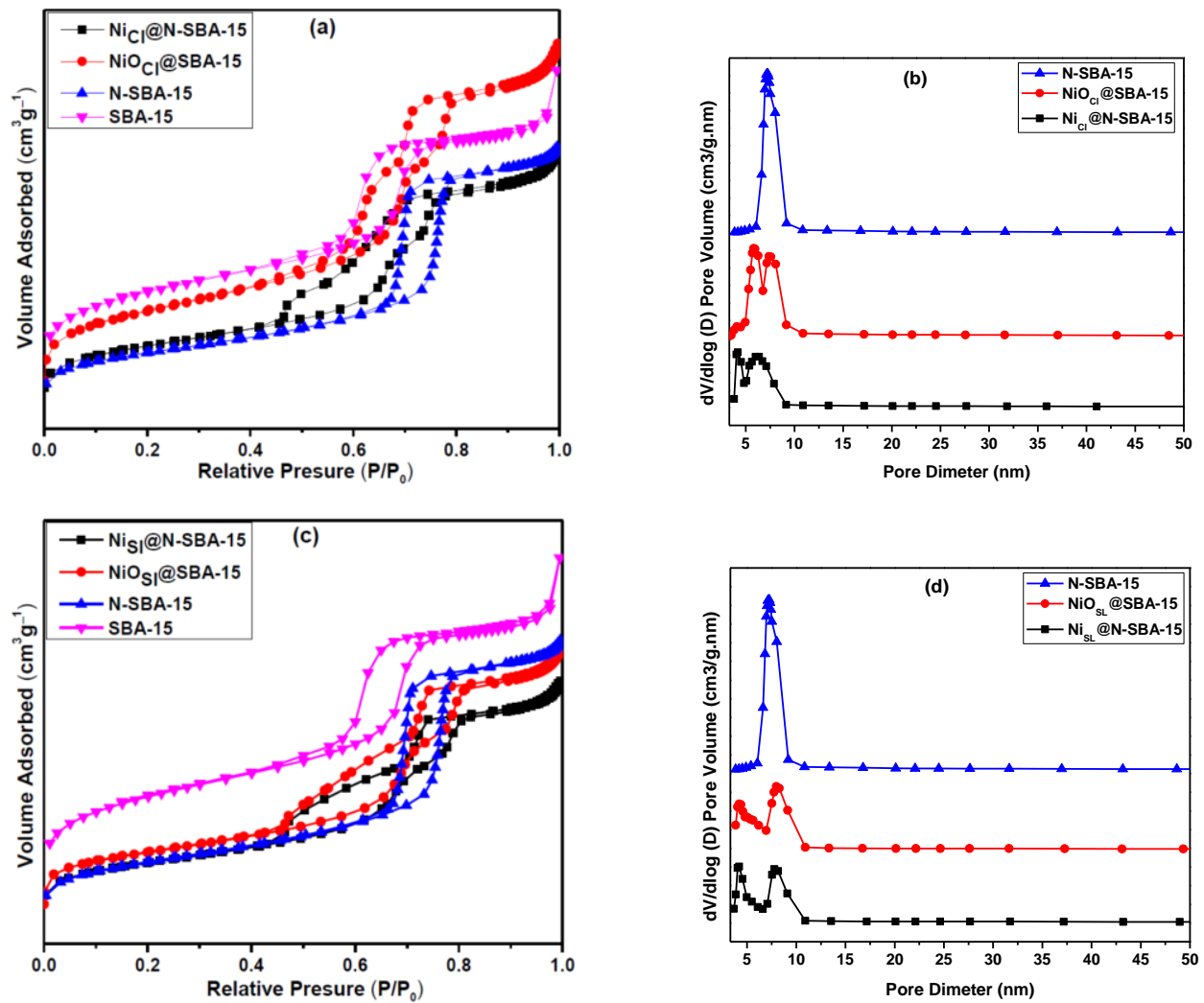


**Figure 4.** N$_2$ physisorption isotherms (**a**,**b**) and pore size distributions (**c**,**d**) of SBA-15, N-SBA-15, [Ni]$_i$@N-SBA-15, and NiO$_i$@SBA-15 (i = Cl and Sl).

**Table 4.** Textural properties of SBA-15, N-SBA-15, [Ni]$_{Ac}$@N-SBA-15, NiO$_{Ac}$@SBA-15, [Ni]$_{Nt}$@N-SBA-15, NiO$_{Nt}$@SBA-15, [Ni]$_{Cl}$@N-SBA-15, NiO$_{Cl}$@SBA-15, [Ni]$_{Sl}$@N-SBA-15, and NiO$_{Sl}$@SBA-15.

| Sample | S$_{BET}$ (m$^2$ g$^{-1}$) | Pore Diameter (nm) | Pore Volume (cm$^3$ g$^{-1}$) |
|---|---|---|---|
| SBA-15 | 715 | 7.70 | 1.24 |
| N-SBA-15 | 342 | 7.20 | 0.78 |
| [Ni]$_{Ac}$@N-SBA-15 | 321 | 4.8 | 0.66 |
| NiO$_{Ac}$@SBA-15 | 450 | 4.8 | 0.86 |
| [Ni]$_{Nt}$@N-SBA-15 | 333 | 6.17 | 0.72 |
| NiO$_{Nt}$@SBA-15 | 434 | 6.17 | 0.81 |
| [Ni]$_{Cl}$@N-SBA-15 | 384 | 5.19 | 0.78 |
| NiO$_{Cl}$@SBA-15 | 607 | 6.69 | 1.05 |
| [Ni]$_{Sl}$@N-SBA-15 | 334 | 6.03 | 0.66 |
| NiO$_{Sl}$@SBA-15 | 391 | 6.17 | 0.74 |

After grafting APTES in the SBA-15 surface and the addition of nickel precursor [Ni]$_i$, followed by the calcination process, N$_2$ physisorption results indicated the preservation of the silica framework and mesoporosity of the prepared materials (N-SBA-15, [Ni]$_i$@N-SBA-15, and NiO$_i$@SBA-15), with typical IV isotherms and an H1 hysteresis loop. The pore size and pore volume of SBA-15 were decreased from 7.70 to 7.20 nm and from 1.24 to 0.78 cm$^3$, respectively, after the grafting reaction of APTES to produce N-SBA-15. (Table 4). After the addition of nickel acetate to N-SBA-15 ([Ni]$_{Ac}$@N-SBA-15), the sharp peak in the pore size distribution curve of N-SBA-15 at 7.20 nm was transformed to a small sharp peak at 4.11 nm, and broad peak at around 5.42 nm (Figure 3b). According to the literature, the small sharp peak and broad peak correspond to narrowed mesopores and open mesopores, respectively (Figure S4) [52]. The apparition of the small sharp peak is probably due to the deposition of nickel acetate at the pore entrance, while the broad peak can be attributed to the increased loading of nickel acetate inside the pores. A similar pores distribution shape was observed after calcination for NiO$_{Ac}$@SBA-15. The BJH average pore diameters of [Ni]$_{Ac}$@N-SBA-15 were found to be around 4.8 nm, which remained approximately the same after calcination for NiO$_{Ac}$@SBA-15 (Table 4). The surface areas and pore volumes of N-SBA-15 (342 m$^2$/g, 0.78 cm$^3$/g) and [Ni]$_{Ac}$@N-SBA-15 (321 m$^2$/g, 0.66 cm$^3$/g) were decreased gradually, with a shift of the capillary condensation step toward lower relative pressures, because of a gradual decrease in the average pore diameter. However, the surface areas and pore volumes were slightly increased again after the calcination process to 450 m$^2$/g, 0.86 cm$^3$/g (NiO$_{Ac}$@SBA-15). This is probably due to the thermal decomposition of nickel acetate tetrahydrate (big molecule) to NiO (small molecule) with the release of water and CO$_2$.

All these findings indicate that APTES and nickel acetate were successfully incorporated into the SBA-15 framework, and nickel acetate was transformed to NiO.

After the addition of nickel nitrate to N-SBA-15, the surface area, average pore diameter, and pore volume of the obtained material ([Ni]$_{Nt}$@N-SBA-15) was decreased to 333 m$^2$/g, 6.17 nm, and 0.72 cm$^3$/g, respectively (Figure 3c,d and Table 4). After the calcination process of [Ni]$_{Nt}$@N-SBA-15 to produce NiO$_{Nt}$@SBA-15, the surface areas and pore volumes were slightly increased to 434 m$^2$/g and 0.81 cm$^3$/g, respectively, with no significant change in the average pore diameter. It should be noted that the pore distribution for [Ni]$_{Nt}$@N-SBA-15 and NiO$_{Nt}$@SBA-15 remains sharp, with no broad peaks and no narrowed mesopores. This can be explained by the small nickel loading, with the absence of nickel deposition at the entrance of the pores in these materials.

When nickel chloride was used as a nickel precursor, the pore size distribution patterns of the obtained materials $[Ni]_{Cl}$@N-SBA-15 and $NiO_{Cl}$@SBA-15 had two main peaks (Figure 4b). This is probably attributed to the deposition of the metal at the pore entrance. In addition, one of these two peaks in the pore distribution pattern of $[Ni]_{Cl}$@N-SBA-15 was broad. This can be attributed to the increased loading of nickel chloride inside the open mesopores. After the calcination process, the broad peak is replaced by a sharp peak; this could be due to the release of $Cl_2$ during the calcination. This can also be confirmed by the increase in the average pore size after calcination from 5.19 nm ($[Ni]_{Cl}$@N-SBA-15) to 6.69 nm ($NiO_{Cl}$@SBA-15) (Table 4). Compared to N-SBA-15, the surface area and pore volume of the obtained material ($[Ni]_{Cl}$@N-SBA-15) were decreased to 384 $m^2/g$ and 0.78 $cm^3/g$, respectively. However, after the calcination process, the surface area, pore size, and pore volume of the obtained material $NiO_{Cl}$@SBA-15 were dramatically increased to 607 $m^2/g$, 6.69 nm, and 1.05 $cm^3/g$, respectively. This could be due to the release of $Cl_2$ (a big molecule compared to $CO_2$ and $NO_2$ in previous precursors).

Using nickel sulfate as a nickel precursor, the surface area, pore size, and pore volume of the obtained material $[Ni]_{Sl}$@N-SBA-15 were decreased to 334 $m^2/g$, 6.03 nm, and 0.66 $cm^3/g$, respectively (Table 4). The pore size distribution pattern of the obtained material $[Ni]_{Sl}$@N-SBA-15 had two main peaks (Figure 4d) corresponding to open and narrowed mesoporous, with an average pore size of 6.03 nm. After the calcination process, the obtained material $NiO_{Sl}$@SBA-15 also showed two main sharp peaks in the pore size distribution pattern, which correspond to narrowed and open mesopores. The surface area, pore size, and pore volume of the final material ($NiO_{Sl}$@SBA-15) were slightly increased to 391 $m^2/g$, 6.17 nm, and 0.74 $cm^3/g$, respectively (Table 4) due to the decomposition of sulfate ions.

Scanning Electron Microscope (SEM)

The particles of amino-functionalized mesoporous silica N-SBA-15 and silica-supported NiO materials $NiO_i$@SBA-15 (i = Ac, Nt, Cl, and Sl) were characterized by SEM to investigate their morphology. Figures 5 and 6 present the obtained micrographs. The SEM images of all materials depict rod-like particles with particles the size of 0.5–2.0 × 0.4 μm and with different aggregation degrees. N-SBA-15 images show a high degree of particle aggregation, with the formation of tubular agglomerates, with different length ranges from 5 to 70 μm (Figure 5a,b). However, after the incorporation of nickel precursors into N-SBA-15 followed by the calcination process, most of the uniform tubular agglomerates of N-SBA-15 were changed to smaller agglomerates of $NiO_i$@SBA-15 with irregular shapes and different size ranges from 1 to 30 μm (Figure 6). This is due to the absence of intermolecular hydrogen bonds, which were present in N-SBA-15 between amines and silanol groups.
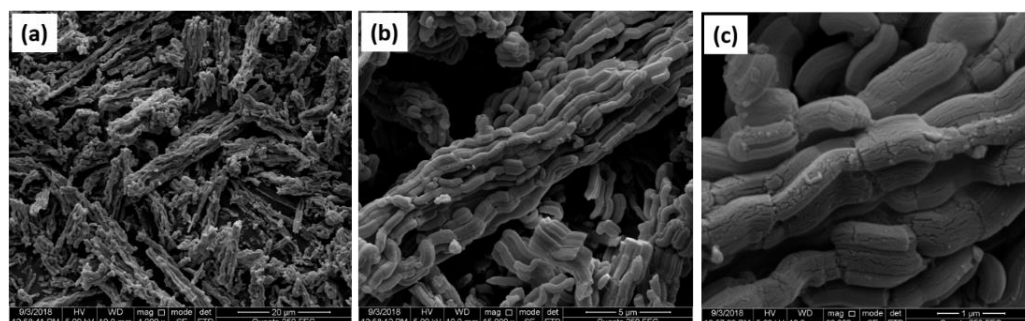


**Figure 5.** SEM images of N-SBA-15 at different magnification. (**a**) 20 μm, (**b**) 5 μm, and (**c**) 1 μm.
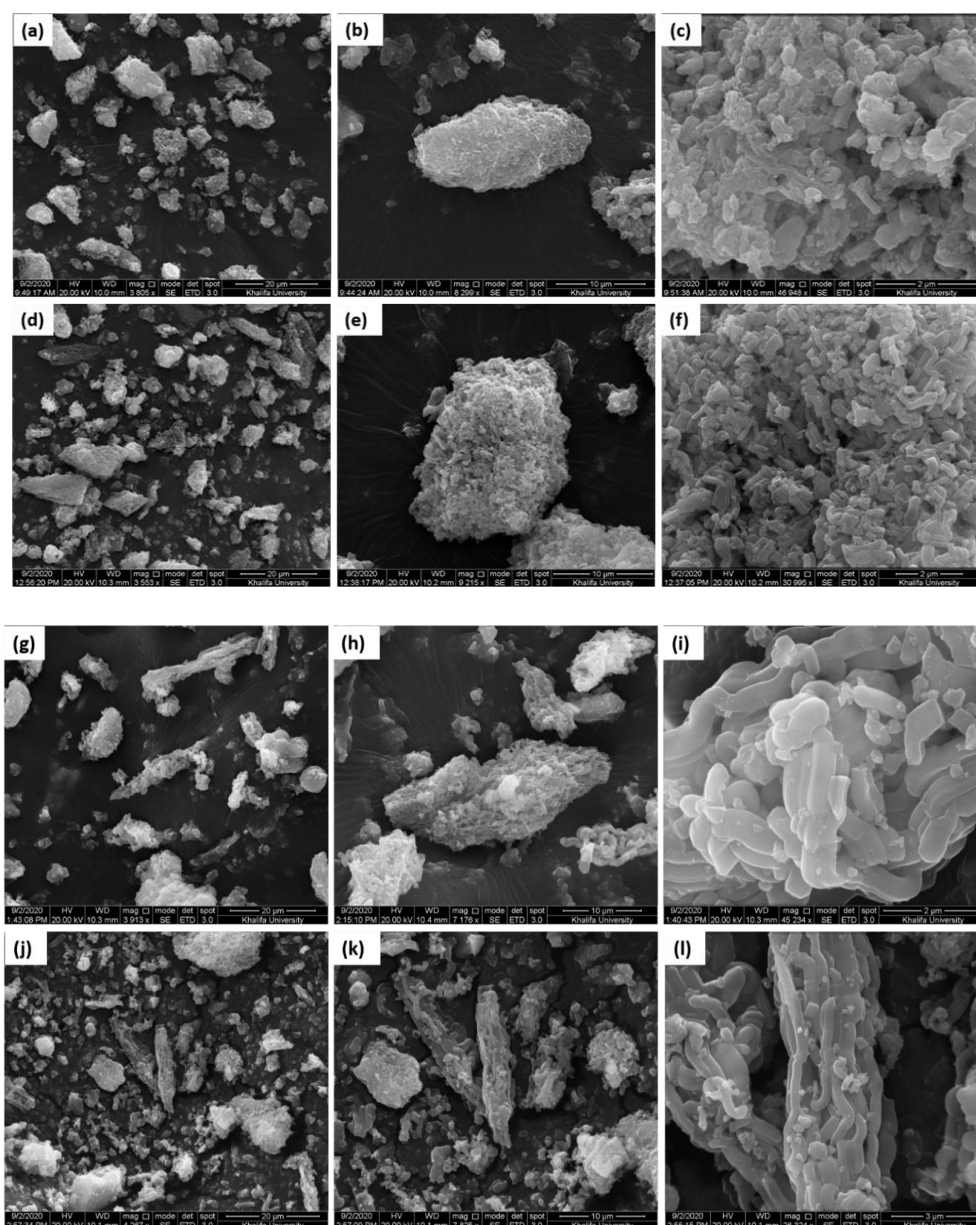
**Figure 6.** SEM images of four nanocatalysts NiO$_i$@SBA-15, with i = Ac (**a–c**), Nt (**d–f**), Cl (**g–i**), and Sl (**j–l**).

Transmission Electron Microscopy (TEM)

Figures 7 and 8 show TEM images of NiO$_i$@SBA-15 materials (i = Ac, Nt, Cl, and Sl). Enlarged TEM images of all materials, except that obtained from nickel chloride (NiO$_{Cl}$@SBA-15), exhibited mono-dispersion of NiO NPs into the SBA-15 surface. Despite the fact that the nickel content in NiO$_{Ac}$@SBA-15 (ca. 7.26%) is high compared to other materials, NiO NPs in this material were highly dispersed. However, enlarged images of NiO$_{Cl}$@SBA-15 (Figure 8a–c) show low dispersion of NiO NPs into silica framework compared to the other three materials. These results are compatible with the XRD patterns (Figure 2), which showed the presence of a crystalline phase of NiO in NiO$_{Cl}$@SBA-15 material, with the absence of any crystalline phase in the other three materials. Similar results were observed previously by Kaydouh et al. [51]. This was probably due to the low solubility of nickel chloride in EtOH. The NiO particle size distribution into NiO$_{Cl}$@SBA-15 was analyzed by *ImageJ* software. The obtained results are illustrated in Figure S5. The NiO NPs diameter in NiO$_{Cl}$@SBA-15 ranges from 3 to 8 nm, with an average diameter

of about 5.53 nm. TEM images indicant the preservation of the structural integrity of the SBA-15 matrix for all samples after the APTES grafting and the calcination process. The enlarged TEM images of NiO$_{Sl}$@SBA-15 (Figure 8f), with a perpendicular view, clearly illustrate a uniform distribution of ultra-fine NiO NPs (black spots) into the honeycomb-like hexagonal mesopores of SBA-15. In addition, the SAB-15 framework was preserved despite the utilization of water as a reaction and washing solvent due to the low solubility of nickel sulfate in EtOH.
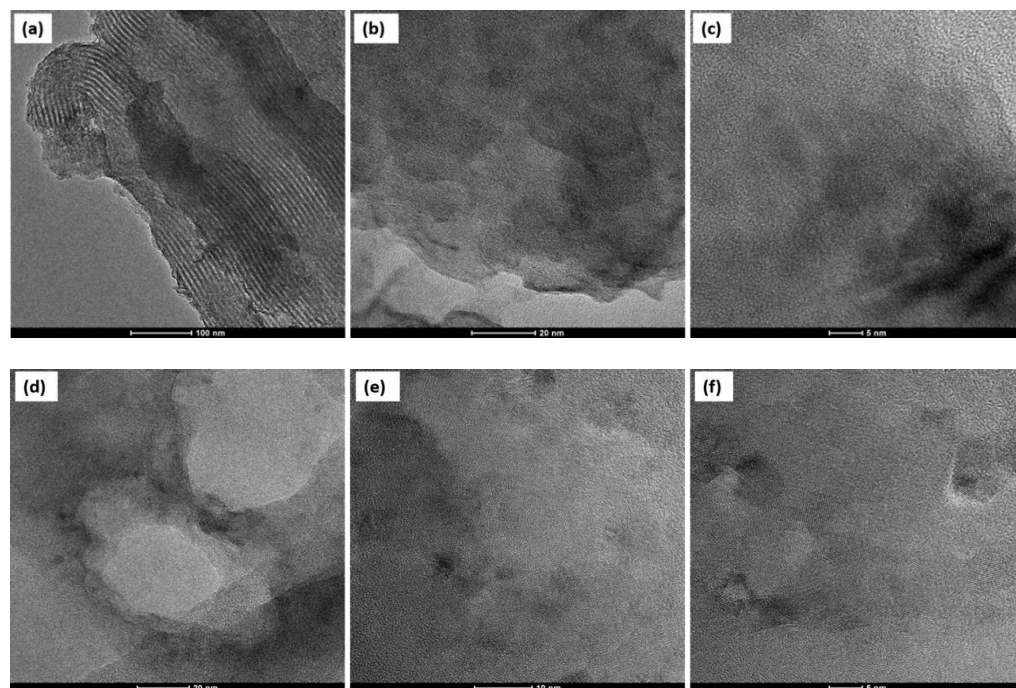


**Figure 7.** TEM images of nanocatalysts NiO$_i$@SBA-15, with i = Ac (**a**–**c**), Nt (**d**–**f**).
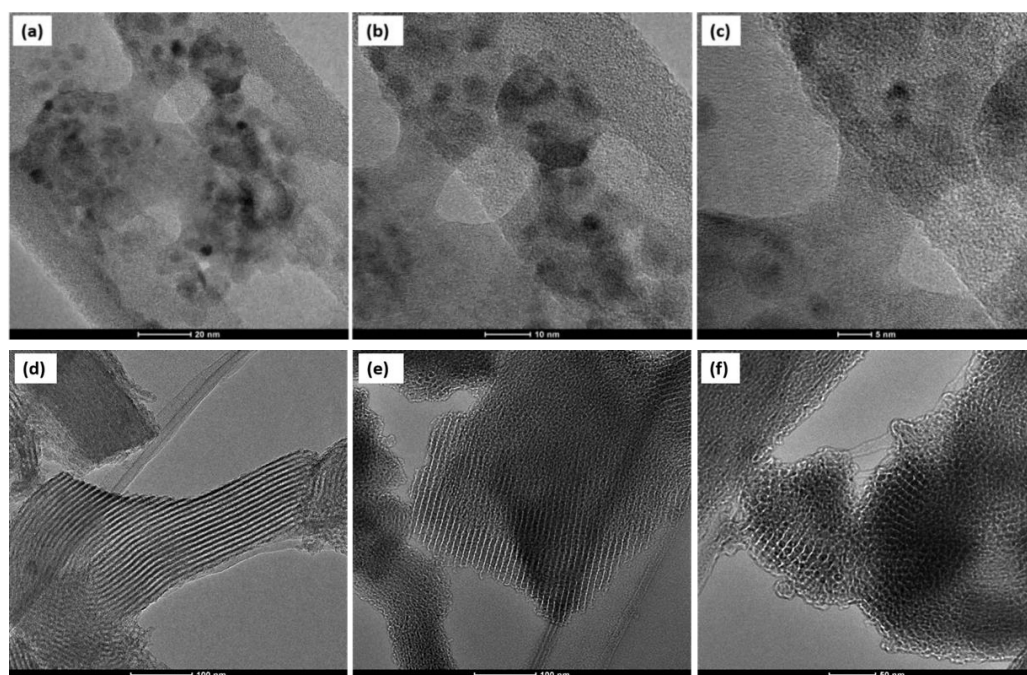


**Figure 8.** TEM images of nanocatalysts NiOi@SBA-15, with i = Cl (**a**–**c**), Sl (**d**–**f**).

### 3.3. Catalytic Activity Evaluation

In order to find the optimal conditions for the oxidation reaction of CXN over SBA-15 supported NiO NPs nanocatalyst (NiO$_i$@SBA-15), and for comparison purposes, unsupported bulk NiO (prepared by calcination of nickel nitrate 5 h at 500 °C) was used as a catalyst for the optimization study. The obtained results were reported recently by Abboud et al. [48]. The highest conversion of cyclohexane and highest selectivity toward KA oil over bulk NiO were obtained using 1.5 eq of *m*-CPBA as an oxidant, with 50 mg of bulk NiO at 70 °C for 24 h, in acetonitrile as a solvent. Compared to various catalysts reported previously, and to the best of our knowledge, for the first time, around 85% of CXN was transformed into products, with 99% KA oil selectivity; this included about 87% and 13% of CXK and CXA, respectively. However, the recyclability study showed low chemical stability of bulk NiO. After five successive runs, the CXN conversion and CXK selectivity were decreased to 63% and 60%, respectively, with a high loss of NiO dose. This is probably due to the decomposition and aggregation of NiO particles.

Therefore, the catalytic activity of the synthesized nanocatalysts NiO$_i$@SBA-15 (i = Ac, Nt, Cl, and St) was evaluated in the oxidation reaction of CXN using the optimized conditions obtained above with unsupported bulk NiO (catalyst: 50 mg; oxidant: *m*-CPBA (1.5 eq); time: 24 h; T = 70 °C, 1 atm). The obtained results are presented in Figure 9. Compared to results obtained with similar amounts of bulk NiO (i.e., 5 and 15 mg of bulk NiO) [48], the conversion of CXN over SBA-15-supported NiO NPs was much higher than that obtained with bulk NiO. A total of 99%, 85%, 75%, and 90% of CXN was converted to KA oil using NiO$_{Ac}$@SBA-15 (Ni: 7.26%), NiO$_{Nt}$@SBA-15 (Ni: 3.66%), NiO$_{Cl}$@SBA-15 (Ni: 4.03%), and NiO$_{Sl}$@SBA-15 (Ni: 5.55%) respectively, compared to 17% and 21% over 5 mg and 15 mg of bulk NiO, respectively. The high conversion obtained with NiO@SBA-15 nanocatalysts compared to bulk NiO is probably due to the higher number of active sites in NiO@SBA-15 materials. In fact, the number of active sites can be increased by decreasing the NiO NPs size. Thus, the lower the NiO particle size, the greater the number of active sites and vice versa. Therefore, the high dispersion of NiO NPs into SBA-15 decreased the particle size and increased the number of active sites, which explains the high conversion of CXN over NiO@SBA-15 nanocatalysts compared to bulk NiO.
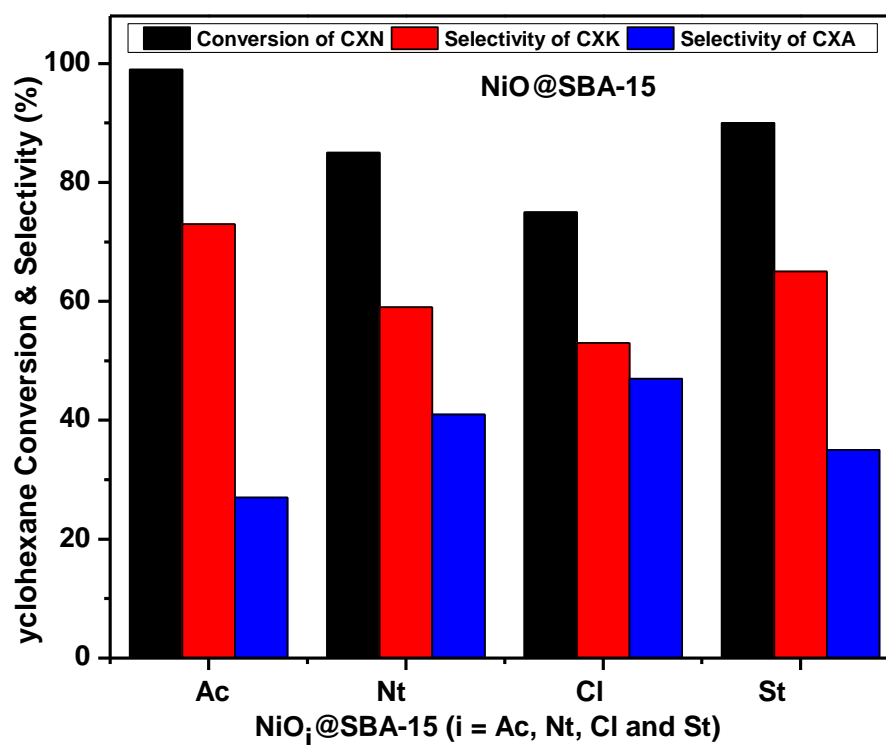


**Figure 9.** Catalytic activity of NiO$_i$@SBA-15 (i = Ac, Nt, Cl, and Sl).

The highest conversion of CXN was obtained with NiO$_{Ac}$@SBA-15. This can be attributed to the mono-dispersion of NiO NPs into SBA-15 and the highest nickel content (Ni: 7.26%) in this catalyst. The conversion of CXN was decreased to 90% and 85% over NiO$_{Sl}$@SBA-15 (Ni: 5.55%) and NiO$_{Nt}$@SBA-15 (Ni: 3.66%), respectively. These results can be explained by the low nickel content in these two nanocatalysts compared to NiO$_{Ac}$@SBA-15 (Ni: 7.26%). However, as expected, the lowest conversion (75%) was obtained with NiO$_{Cl}$@SBA-15 (Ni: 4.03%). This result can be explained by the relative aggregation of NiO NPs, which was clearly observed in the XRD pattern and TEM images of this material (Figures 2 and 8a–c, respectively), in addition to the low nickel content in NiO$_{Cl}$@SBA-15 compared to NiO$_{Ac}$@SBA-15 (Ni: 7.26%) and NiO$_{Sl}$@SBA-15 (Ni: 5.55%).

The CXK and CXA selectivity was also affected by the nickel content and dispersion degree of NiO particles. The highest selectivity toward CXK was obtained with NiO$_{Ac}$@SBA-15 (73%). Further, 65% and 59% selectivity toward CXK were obtained with NiO$_{Sl}$@SBA-15 and NiO$_{Nt}$@SBA-15, respectively. At the same time, only 53% of CXK was obtained when NiO$_{Cl}$@SBA-15 was applied as a catalyst. These results can be explained by the conversion of CXA to CXK over the excess of NiO NPs active sites. Therefore, the higher the nickel content and NiO NPs dispersion, the greater the conversion of CXK to CXA.

Catalyst Recycling Investigation

In order to compare the efficiency of SBA-15-supported NiO NPs nanocatalysts (NiO$_i$@SBA-15) to bulk NiO, the reusability of each catalyst was studied in the same conditions. Due to the higher conversion obtained with the nanocatalysts prepared from the nickel acetate (NiO$_{Ac}$@SBA-15), this material was chosen among the four nanocatalysts prepared in this work to investigate its catalytic activity during four successive runs. After cycle one of the oxidations of CXN, NiO$_{Ac}$@SBA-15 was separated from the reaction mixture by filtration using a centrifuge, then washed with chloroform three times to remove the products and reactants materials, including the formed benzoic acid *m*-CBA after the degradation of *m*-CPBA. After that, the catalyst was dried in the oven at 100 °C to be ready for the next run. This process was repeated after each run. The reaction was monitored by GC to determine the CXN conversion and the products (CXK and CXA) selectivity, according to Equations (1)–(3) mentioned above. The obtained results are plotted in Figure 10.
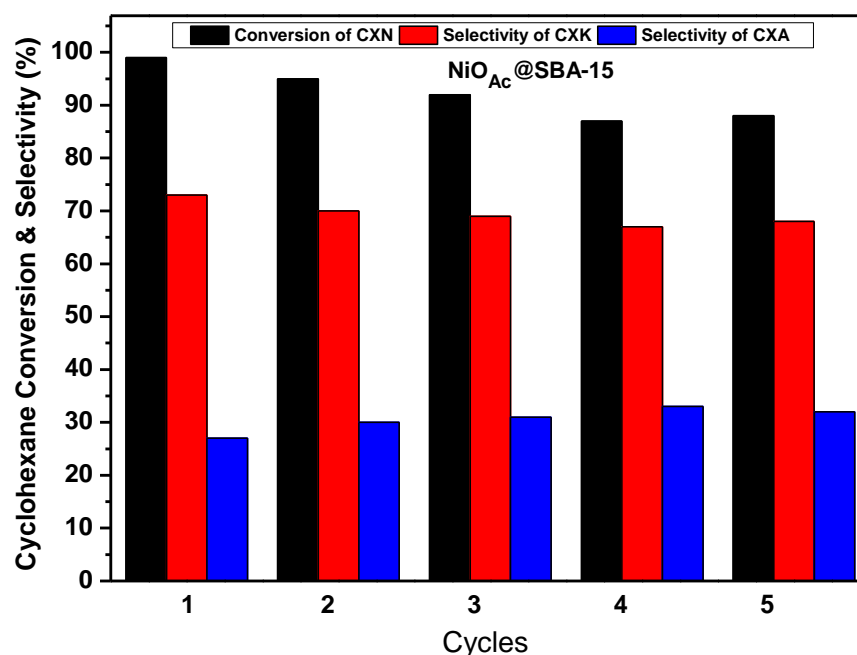


**Figure 10.** Recycling of NiO$_{Ac}$@SBA-15 as a catalyst in the oxidation reaction of CXN using *m*-CPBA as an oxidant. Conditions: Catalyst: NiO$_{Ac}$@SBA-15, 50 mg; Oxidant: *m*-CPBA (1.5 eq), 0.288 g; Solvent: 10 mL of ACN; time: 24 h, T = 70 °C, 1 atm.

In this study, NiO$_{Ac}$@SBA-15 exhibited high stability after four successive runs compared to 5 mg (Figure S6) and 50 mg [48] of bulk NiO. After four cycles, the CXN slightly decreased from 99% to 88%. It should also be noted that the CXK and CXA selectivity was also slightly affected. The selectivity of CXK decreased from 73% to 68%, while the selectivity of CXA increased from 27% to 32%.

### 3.4. Proposed Reaction Mechanism

According to some previous mechanistic studies and theoretical predictions about the oxidation of some hydrocarbons over transition metals [31,53,54], and based on the results obtained in this work, we suggest the mechanism presented in Scheme 2. In this proposed mechanism, we believe that nickel-oxo (O = Ni) and *m*-CBOO• are the active species that can be formed after hemolysis of O-O bond of *m*-CPBA in the presence of silica-supported NiO NPs (Scheme 2, step 1). The formed *m*-CBOO• attacks the C-H bond of CXN to afford CXN• and *m*-CBA (step 2). CXN• species will be oxidized by a second molecule of *m*-CPBA to afford CXA with the formation of another *m*-CBOO• radical (step 3). An amount of CXA will be further oxidized to CXK over O = NiO@SBA-15 (step 4). The CXK/CXA ratio is directly related to the amount of NiO NPs (active) into SBA-15. CXK/CXA ratio increases with the amount of NiO active sites (with high NiO NPs loading and dispersion). The low conversion of CXN to KA oil over *m*-CPBA without a catalyst can be attributed to the slow transformation of *m*-CPBA to *m*-CBOO• radicals (step 5). Moreover, the small CXK/CXA ratio in the absence of the catalyst can be due to the slow oxidation of CXA to CXK over *m*-CPBA (step 6).
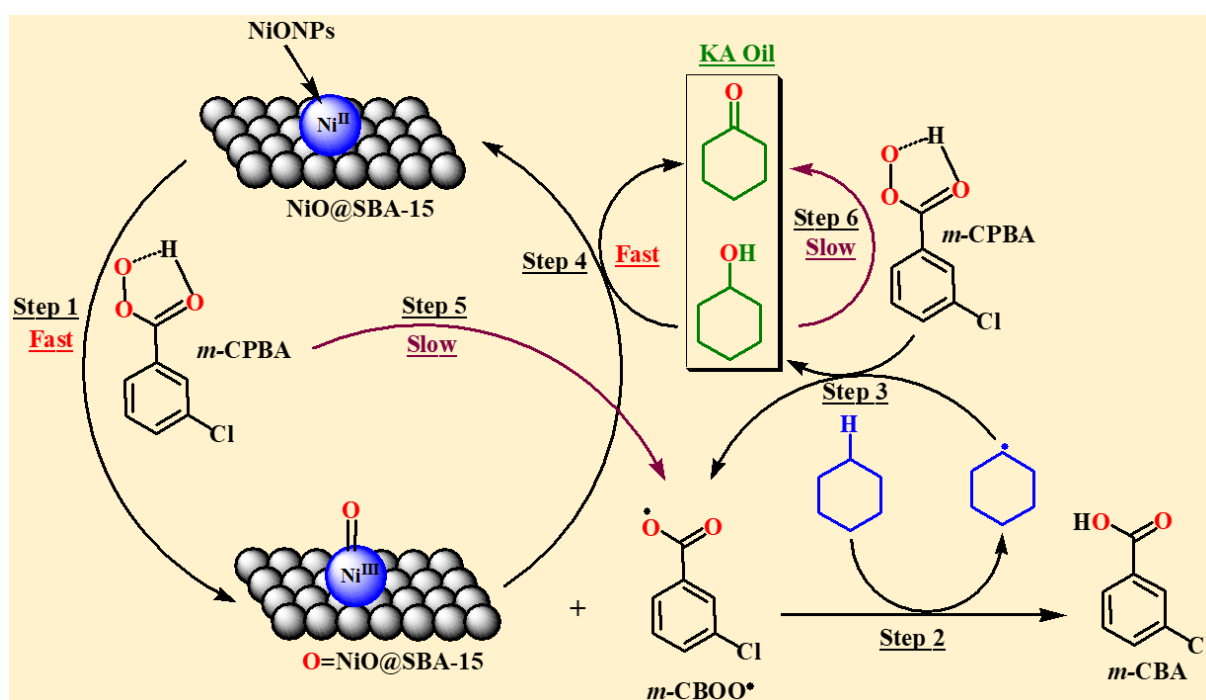


**Scheme 2.** Possible mechanism for the oxidation of cyclohexane over NiO@SBA-15 nanocatalysts.

## 4. Conclusions

In this work, a new approach was developed and applied to prepare highly dispersed NiO NPs supported on SBA-15 mesoporous silica (NiO@SBA-15) from four commercially available nickel precursors, nickel acetate (Ac), nitrate (Nt), chloride (Cl), and sulfate (Sl). This approach, named as coordination-assisted grafting method, consists of immobilizing nickel precursor into amino-functionalized SBA-15 (N-SBA-15) via a coordination bond between the Ni (II) ions and NH$_2$ groups. After removing all free molecules of the nickel precursor by washing with the appropriate solvent, the obtained four catalysts precursors

[Ni]$_i$@SBA-15 (i = Ac, Nt, Cl, or Sl) were calcinated (500 °C, 5 h) to afford the four corresponding nanocatalysts NiO@SBA-15 (i = Ac, Nt, Cl, or Sl). For comparison purposes, bulk NiO was also synthesized by calcination of Ni(NO$_3$)$_2$. 6H$_2$O (500 °C, 5 h) and used as a catalyst. The prepared bulk NiO was also used as a catalyst to optimize the reaction conditions (i.e., oxidant, reaction time, and reaction temperature). The structure, morphology, NiO dispersion, and thermal behavior of the synthesized nanocatalysts were investigated using different techniques, such as HR-TEM, SEM, BET, powder wide-angle XRD, FT-IR, and TGA/DTA. The nickel content in NiO$_i$@SBA-15 nanocatalysts was determined by ICP. The finding revealed high dispersion of NiO NPs into samples prepared from nickel acetate, nitrate, and sulfate. However, the aggregation of NiO particles in the sample prepared from nickel chloride was observed in XRD patterns and TEM images. The catalytic activity performance of these nanocatalysts was investigated in the oxidation reaction of cyclohexane to produce KA oil, using O$_2$, H$_2$O$_2$, TBHP, and *m*-CPBA as oxidants. *m*-CPBA showed exceptional activity compared to other oxidants. The optimized conditions were found to be 1.5 eq of *m*-CPBA at 70 °C for 24 h, in acetonitrile as a solvent. Compared to the previously reported catalytic systems, for the first time, a quantitative conversion (99%) of cyclohexane to KA oil was observed using NiO$_{Ac}$@SBA-15 nanocatalyst, prepared from nickel acetate, with 2.8/1.0 K/A ratio. The catalytic investigation results showed that K/A ratio increases with time and the catalyst dose. The NiO NPs' size, dispersion degree, and catalytic activity were affected by the nature of the nickel precursor and nickel content. Moreover, the reusability of nanocatalysts was also studied. NiO@SBA-15 nanocatalysts exhibited quasi-constant catalytic activity during five successive cycles.

**Supplementary Materials:** The following supporting information can be downloaded at: https://www.mdpi.com/article/10.3390/su15075817/s1, Figure S1. FT-IR spectra of SBA-15 and N-SBA-15; Figure S2. FT-IR spectra of four precursors Nij@N-SBA-15 (j = Ac, Nt, Cl, or Sl); Figure S3. TGA (a) and DTA (b) analysis of precursors [Ni]i@N-SBA-15 (i = Ac, Nt, Cl and Sl); Figure S4. Effect of narrowed pores in the SBA-15 structure on the isotherm shape; Figure S5. Particles diameter distribution in NiOCl@SBA-15; Figure S6. Reusability of bulk NiO powder as a catalyst in the oxidation of CXN with m-CPBA; Table S1. FT-IR peaks of SBA-15, N-SBA-15; Table S2. FTIR data of the catalyst's precursors [Ni]i@N-SBA-15, SBA-15 and N-SBA-15. Reference [53] is cited in Supplementary Materials.

**Institutional Review Board Statement:** Not applicable.

**Informed Consent Statement:** Not applicable.

**Data Availability Statement:** No new data were created.

**Conflicts of Interest:** The authors declare no conflict of interest.

## References

1. Van de Vyver, S.; Román-Leshkov, Y. Emerging catalytic processes for the production of adipic acid. *Catal. Sci. Technol.* **2013**, *3*, 1465–1479. [CrossRef]
2. Sato, K. A "Green" Route to Adipic Acid: Direct Oxidation of Cyclohexenes with 30 Percent Hydrogen Peroxide. *Science* **1998**, *281*, 1646–1647. [CrossRef] [PubMed]
3. Weiping, D.; Longfei, Y.; Binju, W.; Qihui, Z.; Haiyan, S.; Shanshan, W.; Qinghong, Z.; Ye, W. Efficient Catalysts for Green Synthesis of Adipic Acid from Biomass. *Angew. Chem. Int. Ed.* **2021**, *60*, 4712–4719.

4.   Xu, L.; He, C.H.; Zhu, M.Q.; Wu, K.; Lai, Y. Silica-Supported Gold Catalyst Modified by Doping with Titania for Cyclohexane Oxidation. *Catal. Lett.* **2007**, *118*, 248–253. [CrossRef]

5.   Payard, P.A.; Zheng, Y.T.; Zhou, W.J.; Khrouz, L.; Bonneviot, L.; Wischert, R.; Grimaud, L.; Pera-Titus, M. Iron Triflate Salts as Highly Active Catalysts for the Solvent-Free Oxidation of Cyclohexane. *Eur. J. Org. Chem.* **2020**, *24*, 3552–3559. [CrossRef]

6.   Alrufaydi, Z.A.; Ahmed, S.M.; Mubarak, A.T. Synthesis and characterization of novel transition metal complexes with L-Proline and their catalytic activity evaluation towards cyclohexane oxidation. *Mater. Res. Express* **2020**, *7*, 045103. [CrossRef]

7.   Busa, A.V.; Lalancette, R.; Nordlander, E.; Onani, M. New copper (II) salicylaldimine derivatives for mild oxidation of cyclohexane. *J. Chem. Sci.* **2018**, *130*, 59. [CrossRef]

8.   Chen, X.; An, D.L.; Zhan, X.Q.; Zhou, Z.H. 2-Methylimidazole Copper Iminodiacetates for the Adsorption of Oxygen and Catalytic Oxidation of Cyclohexane. *Molecules* **2020**, *25*, 1286. [CrossRef]

9.   Alshaheri, A.A.; Tahir, M.I.M.; Rahman, M.B.A.; Begum, T.; Saleh, T.A. Synthesis, characterisation and catalytic activity of dithiocarbazate Schiff base complexes in oxidation of cyclohexane. *J. Mol. Liq.* **2017**, *240*, 486–496. [CrossRef]

10.   Liu, L.; Arenal, R.; Meira, D.M.; Corma, A. Generation of gold nanoclusters encapsulated in an MCM-22 zeolite for the aerobic oxidation of cyclohexane. *Chem. Commun.* **2019**, *55*, 1607–1610. [CrossRef]

11.   Imanaka, N.; Masui, T.; Jyoko, K. Selective liquid phase oxidation of cyclohexane over $Pt/CeO_2$-$ZrO_2$-$SnO_2/SiO_2$ catalysts with molecular oxygen. *J. Adv. Ceram.* **2015**, *4*, 111–117. [CrossRef]

12.   Hong, Y.; Fang, Y.; Sun, D.; Zhou, X. Ionic liquids modified cobalt/ZSM-5 as a highly efficient catalyst for enhancing the selectivity towards KA oil in the aerobic oxidation of cyclohexane. *Open Chem. J.* **2019**, *17*, 639–646. [CrossRef]

13.   Niu, X.R.; Li, J.; Zhang, L.; Lei, Z.T.; Zhao, X.L.; Yang, C.H. ZSM-5 functionalized in situ with manganese ions for the catalytic oxidation of *cyclohexane*. *RSC Adv.* **2017**, *7*, 50619–50625. [CrossRef]

14.   Lu, X.H.; Yuan, H.X.; Lei, J.; Zhang, J.L.; Yu, A.A.; Zhou, D.; Xia, Q.H. Selective oxidation of cyclohexane to KA-oil with oxygen over active $Co_3O_4$ in a solvent-free system. *Indian J. Chem.* **2012**, *51*, 420–427.

15.   Hong, Y.; Sun, D.; Fang, Y. The highly selective oxidation of cyclohexane to cyclohexanone and cyclohexanol over $VAlPO_4$ berlinite by oxygen under atmospheric pressure. *Chem. Cent. J.* **2018**, *12*, 36. [CrossRef]

16.   Crombie, C.M.; Lewis, R.J.; Kovačič, D.; Morgan, D.J.; Davies, T.E.; Edwards, J.K.; Skjøth-Rasmussen, M.S.; Hutchings, G.J. The Influence of Reaction Conditions on the Oxidation of Cyclohexane via the In-Situ Production of $H_2O_2$. *Catal. Lett.* **2020**, *151*, 164–171. [CrossRef]

17.   Xu, Y.J.; Landon, P.; Enache, D.; Carley, A.F.; Roberts, M.W.; Hutchings, G.J. Selective conversion of cyclohexane to cyclohexanol and cyclohexanone using a gold catalyst under mild conditions. *Catal. Lett.* **2005**, *101*, 175–179. [CrossRef]

18.   Sadiq, M.; Ali, M.; Iqbal, R.; Saeed, K.; Khan, A.; Umar, M.N.; Rashid, H.U. Efficient aerobic oxidation of cyclohexane to ka oil catalyzed by Pt-Sn supported on MWCNTs. *J. Chem. Sci.* **2015**, *127*, 1167–1172. [CrossRef]

19.   Liu, X.; Conte, M.; He, Q.; Knight, D.; Murphy, D.; Taylor, S.; Whiston, K.; Kiely, C.; Hutchings, G.J. Catalytic partial oxidation of cyclohexane by bimetallic Ag/Pd nanoparticles on magnesium oxide. *Eur. J. Chem.* **2017**, *23*, 11834–11842. [CrossRef]

20.   Hong, Y.; Peng, J.; Sun, Z.; Yu, Z.; Wang, A.; Wang, Y.; Liu, Y.Y.; Xu, F.; Sun, L.X. Transition metal oxodiperoxo complex modified metal-organic frameworks as catalysts for the selective oxidation of cyclohexane. *Materials* **2020**, *13*, 829. [CrossRef]

21.   Khirsariya, P.; Mewada, R. Review of a Cyclohexane Oxidation Reaction Using Heterogenous Catalyst. *Int. J. Eng. Dev. Res.* **2014**, *2*, 2321–9939.

22.   Li-Xin, X.; Chao-Hong., H.; Ming-Qiao., Z.; Sheng., F.A. Highly active $Au/Al_2O_3$ catalyst for cyclohexane oxidation using molecular oxygen. *Catal. Lett.* **2007**, *114*, 202–205.

23.   Hao, J.; Wang, J.; Wang, Q.; Yu, Y.; Cai, S.; Zhao, F. Catalytic oxidation of cyclohexane over Ti–Zr–Co catalysts. *Appl. Catal. A-Gen.* **2009**, *368*, 29–34. [CrossRef]

24.   Zhao, H.; Zhou, J.; Luo, H.; Zeng, C.; Li, D.; Liu, Y. Synthesis, characterization of Ag/MCM-41 and the catalytic performance for liquid-phase oxidation of cyclohexane. *Catal. Lett.* **2006**, *108*, 49–54. [CrossRef]

25.   Wu, P.; Bai, P.; Loh, K.P.; Zhao, X.S. Au nanoparticles dispersed on functionalized mesoporous silica for selective oxidation of cyclohexane. *Catal. Today* **2010**, *158*, 220–227. [CrossRef]

26.   Wang, H.; Li, R.; Zheng, Y.; Chen, H.; Wang, F.; Ma, J. An Efficient and Reusable Catalyst of Bismuth-Containing SBA-15 Mesoporous Materials for Solvent-free Liquid Phase Oxidation of Cyclohexane by Oxygen. *Catal. Lett.* **2008**, *122*, 330–337. [CrossRef]

27.   Carneiro, J.T.; Yang, C.C.; Moma, J.A.; Moulijn, J.A.; Mul, G. How gold deposition affects anatase performance in the photo-catalytic oxidation of cyclohexane. *Catal. Lett.* **2009**, *129*, 12–19. [CrossRef]

28.   Ratnasamy, P.; Srinivas, D. Selective oxidations over zeolite-and mesoporous silica-based catalysts: Selected examples. *Catal. Today* **2009**, *141*, 3–11. [CrossRef]

29.   Raja, R.; Ratnasamy, P. Oxidation of cyclohexane over copper phthalocyanines encapsulated in zeolites. *Catal. Lett.* **1997**, *48*, 1–10. [CrossRef]

30.   Li, J.; Li, X.; Shi, Y.; Mao, D.; Lu, G. Selective oxidation of cyclohexane by oxygen in a solvent-free system over lanthanide-containing AlPO-5. *Catal. Lett.* **2010**, *137*, 180–189. [CrossRef]

31.   Hamdy, M.S.; Al-Zaqri, N.; Sahlabji, T.; Eissa, M.; Abu Haija, M.; Alhanash, A.M.; Alsalme, A.; Alharthi, F.A.; Abboud, M. Instant Cyclohexene Epoxidation Over Ni-TUD-1 Under Ambient Conditions. *Catal. Lett.* **2021**, *151*, 1612–1622. [CrossRef]

32. Sahlabji, T.; Abboud, M.; Bel-Hadj-Tahar, R.; Hamdy, M.S. Spontaneous epoxidation of styrene catalyzed by flower-like NiO nanoparticles under ambient conditions. *J. Nanopart. Res.* **2020**, *22*, 364. [CrossRef]

33. Abboud, M.; Alnefaie, R.; Alhanash, A. Unsupported and silica-supported nickel nanoparticles: Synthesis and application in catalysis. *J. Nanopart. Res.* **2022**, *24*, 21. [CrossRef]

34. Jaji, N.D.; Lee, H.L.; Hussin, M.H.; Akil, H.M.; Zakaria, M.R.; Othman, M.B.H. Advanced nickel nanoparticles technology: From synthesis to applications. *Nanotechnol. Rev.* **2020**, *9*, 1456–1480. [CrossRef]

35. Grosso, C.; Boissiere, B.S.; Brezesinski, T.; Pinna, N.; Albouy, P.; Amenitsch, H.; Antonietti, M.; Sanchez, C. Periodically Ordered Nanoscale Islands and Mesoporous Films Composed of Nanocrystalline Multimetallic Oxides. *Nat. Mater.* **2004**, *3*, 787–792. [CrossRef]

36. Lai, T.L.; Lee, C.C.; Wu, K.S.; Shu, Y.Y.; Wang, C.B. Microwave-enhanced catalytic degradation of phenol over nickel oxide. *Appl. Catal. B* **2006**, *68*, 147–153. [CrossRef]

37. Lai, T.L.; Lee, C.C.; Huang, G.L.; Shu, Y.Y.; Wang, C.B. Microwave-enhanced catalytic degradation of 4-chlorophenol over nickel oxides. *Appl. Catal. B* **2008**, *78*, 151–157. [CrossRef]

38. Christoskova, S.T.; Stoyanova, M. Degradation of phenolic waste waters over Ni-oxide. *Water Res.* **2001**, *35*, 2073–2077. [CrossRef]

39. Zou, X.; Conradsson, T.; Klingstedt, M.; Dadachov, M.S.; O'Keeffe, M. A mesoporous germanium oxide with crystalline pore walls and its chiral derivative. *Nature* **2005**, *437*, 716–719. [CrossRef]

40. Ying, J.Y.; Mehnert, C.P.; Wong, M.S. Synthesis and applications of supramolecular-templated mesoporous materials. *Angew. Chem. Int. Ed.* **1999**, *38*, 56–77. [CrossRef]

41. Jia, J.; Wang, Y.; Tanabe, E.; Shishido, T.; Takehira, K. Carbon fibers prepared by pyrolysis of methane over Ni/MCM-41 catalyst. *Microporous Mesoporous Mater.* **2003**, *57*, 283–289. [CrossRef]

42. Basha, S.S.; Sasirekha, N.R.; Maheswari, R.; Shanthi, K. Mesoporous H-AlMCM-41 supported NiO-MoO$_3$ catalysts for hydrodeni-trogenation of o-toluidine: I. Effect of MoO$_3$ loading. *Appl. Catal. A-Gen.* **2006**, *308*, 91–98. [CrossRef]

43. Moreno-Tost, R.; Santamaría-González, J.; Maireles-Torres, P.; Rodríguez-Castellón, E.; Jiménez-López, A. Nickel oxide supported on zirconium-doped mesoporous silica for selective catalytic reduction of NO with NH$_3$. *J. Mater. Chem.* **2002**, *12*, 3331–3336. [CrossRef]

44. Polshettiwar, V.; Baruwati, B.; Varma, R.S. Nanoparticle-supported and magnetically recoverable nickel catalyst: A robust and economic hydrogenation and transfer hydrogenation protocol. *Green Chem.* **2009**, *11*, 127–131. [CrossRef]

45. Alonso, F.; Riente, P.; Yus, M. Nickel nanoparticles in hydrogen transfer reactions. *Acc. Chem. Res.* **2011**, *44*, 379–391. [CrossRef]

46. Abboud, M.; Al-Zaqri, N.; Sahlabji, T.; Eissa, M.; Mubarak, A.T.; Bel-Hadj-Tahar, R.; Alsalme, A.; Alharthi, F.A.; Alsyahi, A.; Hamdy, M.S. Instant and quantitative epoxidation of styrene under ambient conditions over a nickel(ii)dibenzotetramethyltetraaza [14] annulene complex immobilized on amino-functionalized SBA-15. *RSC Adv.* **2020**, *10*, 35407–35418. [CrossRef]

47. Abboud, M.; Sahlabji, T.; Eissa, M.; Bel-Hadj-Tahar, R.; Mubarak, A.T.; Al-Zaqri, N.; Hamdy, M.S. Nickel (II) dibenzotetramethyl-tetraaza [14]annulene complex immobilized on amino-functionalized TUD-1: An efficient catalyst for immediate and quantitative epoxidation of cyclohexene under ambient conditions. *New J. Chem.* **2020**, *44*, 20137–20147. [CrossRef]

48. Alnefaie, R.S.; Abboud, M.; Alhanash, A.; Hamdy, M.S. Efficient Oxidation of Cyclohexane over Bulk Nickel Oxide under Mild Conditions. *Molecules* **2022**, *27*, 3145. [CrossRef]

49. Clavier, H.; Pellissier, H. Recent Developments in Enantioselective Metal-Catalyzed Domino Reactions. *Adv. Synth. Catal.* **2012**, *354*, 3347–3403. [CrossRef]

50. Behnajady, M.A.; Bimeghdar, S. Synthesis of mesoporous NiO nanoparticles and their application in the adsorption of Cr(VI). *Chem. Eng. J.* **2014**, *239*, 105–113. [CrossRef]

51. Kaydouh, M.N.; El Hassan, N.; Davidson, A.; Massiani, P. Optimization of synthesis conditions of Ni/SBA-15 catalysts: Confined nanoparticles and improved stability in dry reforming of methane. *Catalysts* **2021**, *11*, 44. [CrossRef]

52. Thielemann, J.P.; Girgsdies, F.; Schlögl, R.; Hess, C. Pore structure and surface area of silica SBA-15: Influence of washing and scale-up. *Beilstein J. Nanotechnol.* **2011**, *2*, 110–118. [CrossRef] [PubMed]

53. Kooti, M.; Afshari, M. Phosphotungstic acid supported on magnetic nanoparticles as an efficient reusable catalyst for epoxidation of alkenes. *Mater. Res. Bull.* **2012**, *47*, 3473–3478. [CrossRef]

54. Dmytro, S.; Oksana, V.N. Catalytic Oxidations with Meta-Chloroperoxybenzoic Acid (*m*-CPBA) and Mono-and Polynuclear Complexes of Nickel: A Mechanistic Outlook. *Catalysts* **2021**, *11*, 1148.